Refractive index reconstruction using optical diffraction tomography algorithms based on single-scattering and multiple-scattering models

Meng Lip Lim [a], Álvaro Fernández Galiana [a], Patrick Salter [a], Martin Booth [a*]

[a] Department of Engineering Science, University of Oxford, United Kingdom

[*] martin.booth@eng.ox.ac.uk; phone +441865612718

ABSTRACT

Optical diffraction tomography is a popular technique used to retrieve the refractive index (RI) distribution of transparent and refractive specimens. Conventional tomography algorithms based on the first-order Born and Rytov approximations are commonly employed, but are limited to optically thin specimens due to the single-scattering assumption. Tomography reconstruction algorithms incorporating multiple-scattering models can overcome this limitation. However, their iterative nature increases computational cost, making them less suitable for applications requiring higher computational efficiency. In this study, the reconstruction accuracy of two intensity-based optical diffraction tomography algorithms was compared: a transport-of-intensity equation (TIE)-based algorithm that employed a single-scattering model and a Fourier beam propagation (FBP)-based algorithm that incorporated a multiple-scattering model. Both algorithms were applied to reconstruct the RI cross-section of a single-mode fibre core. In addition, two FBP-based reconstruction approaches were compared: digital illumination rotation and digital specimen rotation. The results show that the TIE-based algorithm provides good reconstruction accuracy, but requires additional measures to suppress reconstruction artefacts. The FBP-based algorithm yields higher accuracy, and the digital specimen rotation approach produces more accurate results than the digital illumination rotation approach.

Keywords: refractive index, tomography, single-scattering, multiple-scattering

1. INTRODUCTION

The ability to image transparent specimens is important for numerous applications, such as biological cell imaging [1, 2] and inspection of transparent products in manufacturing [3, 4]. This task is challenging, however, because transparent specimens produce weak intensity contrast due to low optical absorption. The needs to clearly visualise transparent specimens has led to the development of various qualitative phase imaging techniques, such as phase contrast microscopy and differential interference contrast microscopy. More recently, quantitative phase imaging methods have been developed, enabling the measurement of physical properties of transparent specimens, such as geometry and refractive index (RI).

By combining quantitative phase imaging with tomography, these properties can be reconstructed in higher-dimension domains. Conventionally, such information is reconstructed using tomography algorithms based on the Fourier projection or diffraction theorems, which relate the Fourier spectrum of the scattered light field to that of the scattering potential. These algorithms provide exact analytical solutions, but are computationally difficult and expensive to implement. To simplify the problem, the Born or Rytov approximations are commonly employed, but they assume weak and single-scattering of light by the specimen.

To account for multiple scattering, particularly in thicker specimens with higher RI variation, several multi-slice reconstruction methods have been developed. In these approaches, the specimen is divided into multiple slices. An initial light field, typically assumed to be a plane wave, is propagated sequentially through the slices until it reaches the camera focus plane. Various propagation algorithms have been used, including the beam propagation method [5], the wave propagation method [6], and the multi-layer Born method [7]. The intensity of the propagated field is compared with the

measured intensity, and the difference is used to iteratively update the specimen properties using optimisation algorithms based on gradient descent.

In this study, tomographic reconstruction algorithms were used to measure the RI cross-sections of a single-mode fibre core. It is known that the reconstruction algorithms based on multiple-scattering models yield higher accuracy than those based on single-scattering models. However, the iterative operation significantly increases computational time, making them less suitable for application requiring fast and reasonably accurate results, such as online measurement of the RI cross-sections. In contrast, single-scattering models are computationally efficient, but their accuracy for this applications remains uncertain.

The objective of this paper is to investigate the accuracy performance of tomographic reconstruction algorithms based on single-scattering and multiple-scattering models. The single-scattering model is implemented using the transport-of-intensity equation (TIE)-based method [8], while the multiple-scattering model is implemented using a Fourier beam propagation (FBP)-based method. Both methods use intensity-only measurements to reconstruct RI cross-sections, thereby greatly reducing the hardware complexity of the measurement system.

2. METHODOLOGY

2.1. TIE-based tomography

Equation (1) shows the transport-of-intensity equation (TIE), which is derived by solving the paraxial wave equation and taking the imaginary part of the solution [9]. The variables ϕ and I denote the phase and intensity of the light field, respectively. The variable ∂I/∂z denotes the axial intensity gradient along the direction of light propagation, which is the z-direction in this equation. The operators $\nabla_\perp \bullet$ and $\nabla_\perp$ are the divergence and gradient operators, respectively. The variable $\bar{k}$ is the average wave number of light propagating through the specimen, as shown in Equation (2). Here, $\bar{n}$ denotes the average RI and λ_0 denotes the wavelength of light in free space.

$$-\bar{k}\frac{\partial I}{\partial z} = \nabla_\perp \bullet \left[I \nabla_\perp \phi\right] \tag{1}$$

$$\bar{k} = \frac{2\pi\bar{n}}{\lambda_0} \tag{2}$$

By assuming that the transverse energy flux $I \nabla_\perp \phi$ is conservative, the solution to the TIE is given in Equation (3). The operator $\nabla_\perp^{-2}$ is the inverse Laplacian. Since the RI distribution and the thickness of the specimen were unknown during measurement, the average wave number $\bar{k}$ was also unknown. By assuming that $\bar{k}$ in Equation (3) was equal to the wave number in the immersion medium k_m, the accumulated phase ϕ across the specimen was estimated. This assumption only valid for optically thin specimens.

$$\phi = -\bar{k}\, \nabla_\perp^{-2} \nabla_\perp \bullet \left[\frac{1}{I} \nabla_\perp \nabla_\perp^{-2} \frac{\partial I}{\partial z}\right] \tag{3}$$

Based on scalar diffraction theory, the total light field $u_t(\vec{r})$ is constructed using the measured intensity I and the accumulated phase ϕ computed using the TIE, as shown in Equation (4). The scattered light field $u_s(\vec{r})$ was then computed using Equation (5), where $u_i(\vec{r})$ denotes the incident light field, which was assumed to be a plane wave.

$$u_t(\vec{r}) = \sqrt{I} e^{j\phi} \tag{4}$$

$$u_s(\vec{r}) = u_t(\vec{r}) - u_i(\vec{r}) \tag{5}$$

The scattered light field $u_s(\vec{r})$ is related to its scattering potential $s(\vec{r})$, which contains information about the RI distribution of the the specimen, as shown in Equation (6). This equation cannot be solved directly. Thus, the first-order Born approximation is used to simply the problem, by assuming that the first-order solution $u_B(\vec{r})$ is equal to the scattered field $u_s(\vec{r})$. Alternatively, the Rytov approximation can also be used, and the relationship between its solution $u_R(\vec{r})$ to $u_B(\vec{r})$ is given in Equation (7).

$$u_B(\vec{r}) = u_s\vec{r} = \int g(\vec{r} \mid \vec{r}')\ s(\vec{r}')\ u_i(\vec{r}')\ d\vec{r}' \tag{6}$$

$$u_R(\vec{r}) = u_i(\vec{r})\ \left[e^{\frac{u_B(\vec{r})}{u_i(\vec{r})}} - 1\right] \tag{7}$$

For specimens with the cross-sectional dimensions to be infinite in extent, the Green's function that solves the 2D partial differential equations is a zero-order Hankel function of the first kind that describes the plane wave decomposition of a cylindrical wave. By substituting the Green's function into Equation (6), the 2D diffraction tomography algorithm is obtained, as shown in Equation (8). Here, S denotes the Fourier transform of the scattering potential $s(\vec{r})$, k_u denotes the angular frequency, Δd denotes the defocus distance between the camera focus plane and the illumination rotation axis, and U_s denotes the Fourier transform of the first-order scattered field $u_B(\vec{r})$ or $u_R(\vec{r})$. The cross-section of RI variation $\Delta n(\vec{r})$ of the specimen was then reconstructed using Equation (9), where n_m denotes the RI of the immersion medium.

$$S\left(k_u, \sqrt{k_m^2 - k_u^2} - k_m\right) = \left[-j\sqrt{\frac{2(k_m^2 - k_u^2)}{\pi}} e^{j(\sqrt{k_m^2 - k_u^2} - k_m)\Delta d}\right] U_s(k_u) \tag{8}$$

$$\Delta n(\vec{r}) = n_m\sqrt{\frac{s(\vec{r})}{k_m^2} + 1} - n_m \tag{9}$$

2.2. FBP-based tomography

Fourier beam propagation (FBP) is a class of beam propagation methods that solves the light propagation equation using Fourier transforms. The method models light propagation in an inhomogeneous medium by separating the propagation into two components. The diffraction component simulates propagation in a homogeneous medium, whereas the refraction component models phase modulation by a thin inhomogeneous layer. Given the Δn of the specimen at each slice z and an initial light field, the light fields at subsequent slices were computed sequentially. Equation (10) shows the formula of the FBP-based method, where Δz denotes the length of the propagation step.

$$u(z + \Delta z) = F^{-1}\left[F[u(z)]e^{j\sqrt{k_m^2 - k_u^2}\Delta z}\right] e^{-jk_0\Delta n(z)\Delta z} \tag{10}$$

For tomographic reconstruction, the illumination light was propagated at various angles θ_i. Thus, oblique factors were introduced to modify Equation (10), resulting in Equation (11). An oblique factor was applied to the diffraction term to shift the spatial frequency, and another to the refraction term to account for the increased length of the propagation step Δz.

$$u(z + \Delta z) = F^{-1}\left[F[u(z)]e^{j\sqrt{k_m^2 - (k_u - k_m\sin(\theta_i))^2}\Delta z}\right] e^{\frac{-jk_0\Delta n(z)\Delta z}{\cos(\theta_i)}} \tag{11}$$

Figure 1(a) shows an example of the normalised intensity of light propagated through a standard single-mode fibre core (Thorlabs: SMF28) with Δn of 0.0067, simulated using Equation (11). The illumination angle is set to 54°, which is close to the maximum illumination angle in the experimental setup.

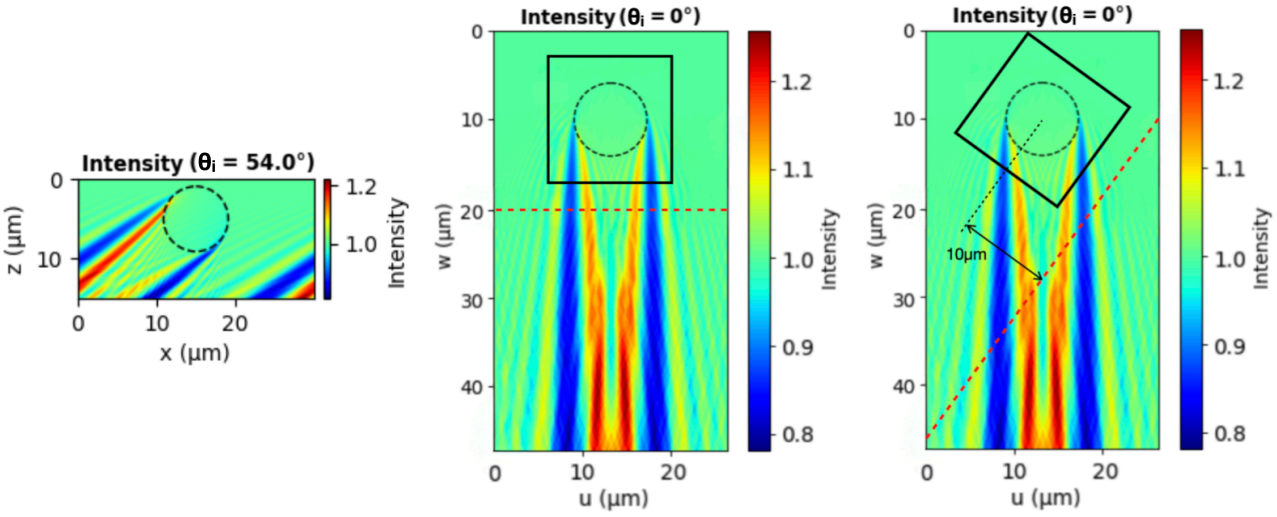

(a) (b) (c)

Figure 1: (a) Intensity of the light field simulated using digital illumination rotation approach. Intensity of the light field, when the illumination angle is (a) 0° and (b) 54°, simulated using the digital specimen rotation approach.

Owing to the periodic boundary condition when using FBP-based algorithms, the light field shown in Figure 1(a) is wrapped around the left and right edges of the computational window. This can be mitigated by increasing the width of the window until the light field at both edges remain essentially undisturbed. A non-symmetric intensity distribution is observed along the propagation axis in Figure 1(a), even though the simulated specimen is rotationally symmetric. The main cause of this issue is paraxial approximation, which causes the accuracy of the algorithm to degrade as the illumination angle θ_i increases. To address this issue, an FBP-based tomographic reconstruction algorithm that digitally rotates the specimen instead of the illumination angle was developed [10].

Figures 1(b) and 1(c) show the intensity of the propagated field for θ_i = 0° and θ_i = 54°, respectively. In Figure 1(b), the window containing the specimen, indicated by the black box, is not rotated. The intensity of the light field at the camera focus plane is extracted along the profile indicated by the red dashed line. In Figure 1(c), the illumination angle is 54°. Therefore, the specimen window is rotated by the same angle in the opposite direction. To maintain a consistent defocus distance Δd, the profile used to extract the intensity of the light field is also rotated by the same angle. Using this approach, the light field is always propagated along the axial direction with a constant propagation step Δz.

For iterative reconstruction, the RI cross-section of the specimen was first initiated as zero. The FBP-based method was then applied to simulate forward light propagation using Equation (10). By comparing the intensities of the propagated light field I and the measured light field $\hat{I}$ for samples at the different illumination angles, the mean-batch sum-squared intensity loss was computed, as shown in Equation (12). Here, L_T denotes the total loss, b denotes the batch index, B denotes the batch number (fixed as 8 in our study), n denotes the sample index, and N denotes the maximum number of samples in a batch. Using the adaptive moment estimation (ADAM) optimiser with a learning rate of 0.001, the computed loss gradient is back-propagated through the cross-section to update the Δn values. This iteration was terminated when L_T increased for 10 epochs consecutively after reaching a minimum.

$$L_T = \frac{1}{B}\sum_{b=0}^{B}\sum_{n=0}^{N}(I_n - \hat{I}_n)^2 \tag{12}$$

2.3. Experimental setup

Figure 2 shows the limited-angle tomography system used in the study. A fibre-coupled light-emitting diode (Thorlabs, M617F1), producing light with a wavelength of 617 nm, was used as the illumination source. The output light was collimated and directed onto a one-dimensional galvanometer mirror (Thorlabs, GVS011), which reflected the beam towards a focusing lens (Thorlabs, AC-508-150AB-ML). The light was focused onto the back aperture of a condenser (Olympus, U-AAC) before transmitting through the specimen mounted on the specimen stage. Owing to the 4-*f* configuration between the galvanometer mirror and the specimen at the focus plane, rotation of the mirror caused the illumination beam to rotate about the specimen. The transmitted light was subsequently collected and relayed onto a camera sensor by another 4-*f* optical system. This system employed an infinity-corrected objective lens (Olympus: UPlanSApo 100×/ 1.40 oil) and a tube lens (Thorlabs: AC-180-AB-ML). During the experiments, both the condenser and the objective lens were immersed in oil (Leica, n_e = 1.518).

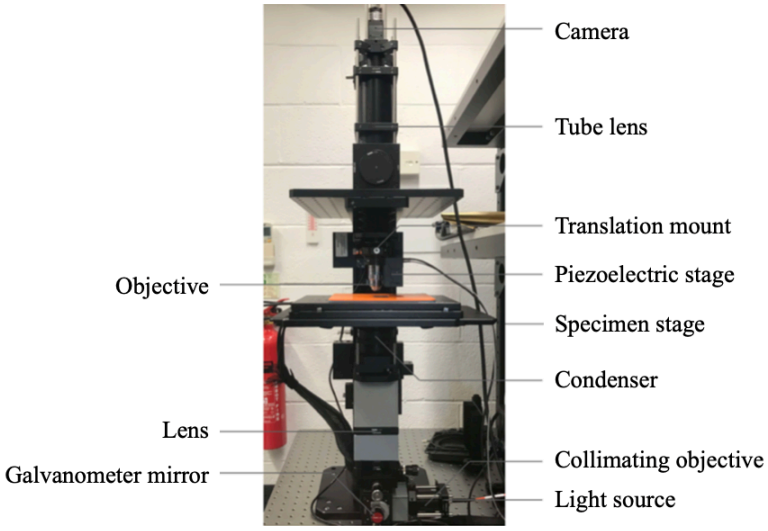

Figure 2: Experimental setup for the developed tomography system.

3. RESULTS AND DISCUSSION

3.1. TIE-based tomographic measurement

In this study, the RI cross-section of a single-mode fibre core (Thorlabs: SMF28) was measured using the developed tomography system. A single-mode fibre was selected as the specimen because it has a well-defined cylindrical shape and RI distribution. The input voltage applied to the galvanometer mirror was varied from -2.0 V to 2.0 V in increments of 0.01 V, corresponding to an illumination angle range of approximately -54° to 54°. Images of the fibre core were captured at a defocus distance of 10μm above the illumination rotation centre for each illumination angle. An intensity sinogram was obtained by averaging rows of the fibre core images, as shown in Figure 3(a).

A shift in the fibre core position along the distance x with illumination angle is observed in Figure 3(a). Since the illumination angles were well calibrated, this shift was corrected using trigonometry, and the resulting sinogram is shown in Figure 3(b). The broadening of the fibre core image with increasing illumination angle is evident in Figure 3(b). This broadening effect should be corrected to ensure a constant defocus distance for accurate TIE-based phase retrieval. In practice, the actual intensity distribution on the imaginary plane differs from the interpolated intensity, and larger phase errors are expected at higher illumination angles or for specimens with more complex RI distributions. By interpolating

the captured intensity at the focus plane onto an imaginary plane perpendicular to the illumination direction, the broadening effect is reduced, as shown as the result in Figure 3(c).

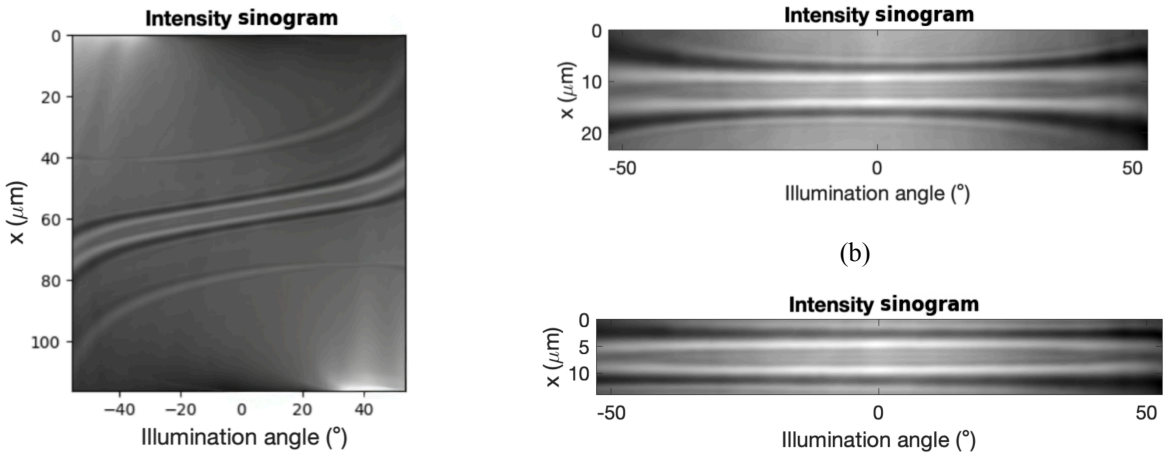

(a) (b) (c)

Figure 3: (a) Original sinogram. Sinogram after correcting (b) the shifting effect and (c) the shifting and broadening effects.

By applying the TIE in Equation (3), the accumulated phase of the specimen at each illumination angle was computed from the intensity sinogram in Figure 3(c). The axial intensity gradient required for TIE was estimated using a forward finite difference method to reduce image acquisition and computational time. The resulting phase sinogram is shown in Figure 4. The phase sinogram shows good consistency across illumination angles, as expected for a rotationally symmetric fibre core.

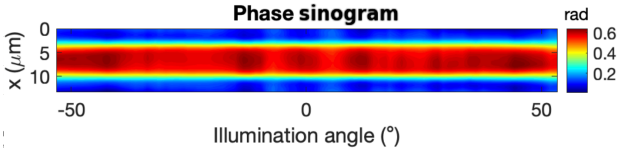

Figure 4: Phase sinogram.

Figures 5(a) and 5(b) show the RI cross-section reconstructed using optical diffraction tomography with the first-order Born and Rytov approximations, respectively. Figure 5(c) compares the theoretical and the measured RI profiles extracted along the centre row of the RI cross-sections. In Figures 5(a) and 5(b), the reconstructed RI cross-sections exhibit circular shapes that are slightly elongated along the z -direction due to the missing cone problem. Reconstruction artefacts are present in both cases, and the edges of the fibre cores appear blurred. The plot in Figure 5(c) shows that the RI profiles of the fibre core fluctuate within a range of approximately 0.006 to 0.009. Overall, the RI cross-sections reconstructed using the TIE-based method exhibit the correct geometry and a reasonable range of RI values.

3.2. FBP-based tomographic measurement

To investigate the performance of the FBP-based tomographic reconstruction algorithm under ideal imaging conditions free from random and systematic intensity distortions, the measured intensity data I was replaced with simulated intensity data I_s generated using the FBP model. Figures 6(a) and 6(b) show the measured and the simulated

intensity sinograms, respectively. Figure 6(c) shows the sum-squared error between the measured and the simulated intensity sinograms as a function of illumination angles.

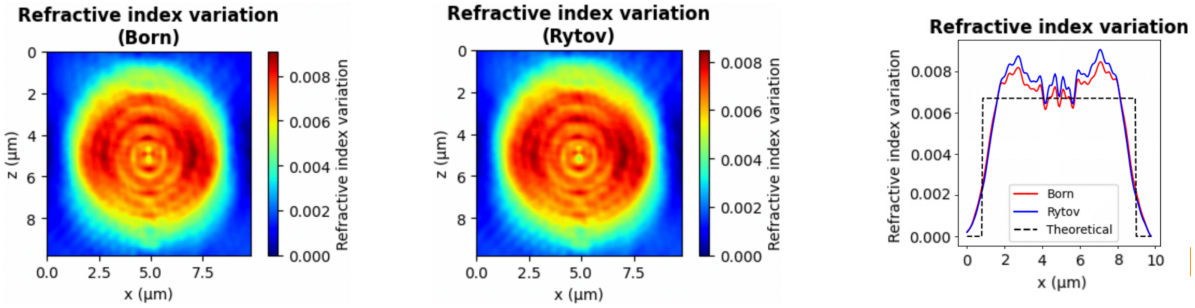

(a) (b) (c)

Figure 5: RI cross-section computed using diffraction tomography based on the (a) Born and (b) Rytov approximation. (c) The theoretical and measured RI profiles of the fibre core.

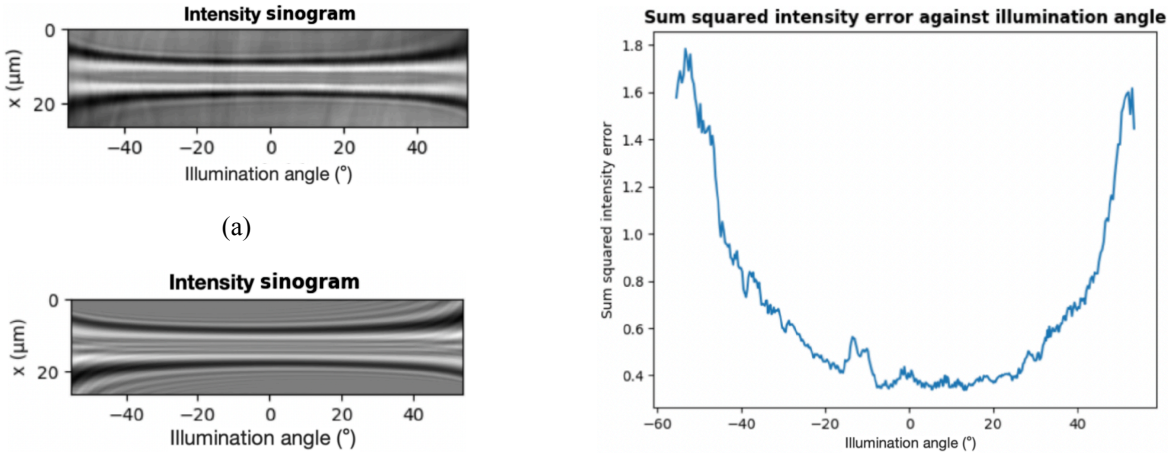

(a)

(b) (c)

Figure 6: (a) Measured and (b) simulated intensity sinograms. (c) Sum-squared error between the measured and the simulated sinograms at different illumination angles.

Comparison of Figures 6(a) and 6(b) shows that the simulated sinogram closely resembles the measured one, differing mainly in a cleaner background. This agreement indicates that the forward FBP model accurately describes the light propagation, and suggests that the inverse FBP-based reconstruction should perform well under ideal conditions. Figure 6(c) shows that the sum-squared intensity error increases with increasing magnitude of illumination angle, indicating the presence of systematic distortions. Possible sources of these errors include: (i) optical aberrations in the imaging system at large illumination angles, and (ii) specimen-induced aberrations from the fibre cladding, which was assumed to have the same RI as the immersion medium to simplify the computation.

Figures 7(a) and 7(b) show the RI cross-sections of the fibre core reconstructed from the simulated and measured intensity sinograms, respectively, using the digital illumination rotation method. Figures 7(c) and 7(d) show the corresponding reconstructions obtained using the digital specimen rotation method. Comparison of Figures 7(a) and 7(b) shows that the maximum-to-minimum Δn is roughly similar in both reconstructions. However, the reconstruction obtained using the simulated intensity data exhibits substantially higher quality. The reconstruction in Figure 7(b) is corrupted by artefacts, having blurred edges and is elongation along the z-direction due to the missing cone problem. An

uneven background is observed in both Figures 7(a) and 7(b). Comparing Figures 7(a) and 7(c), the background flatness is improved when the digital specimen rotation method is used. Similarly, comparison of Figures 7(b) and 7(d) shows that the circularity of the reconstructed RI cross-section is enhanced using this method. Nonetheless, the edge of the RI cross-section in Figure 7(d) remains indistinct, possibly due to noise around the edges of the reconstruction window which reduces the image contrast.

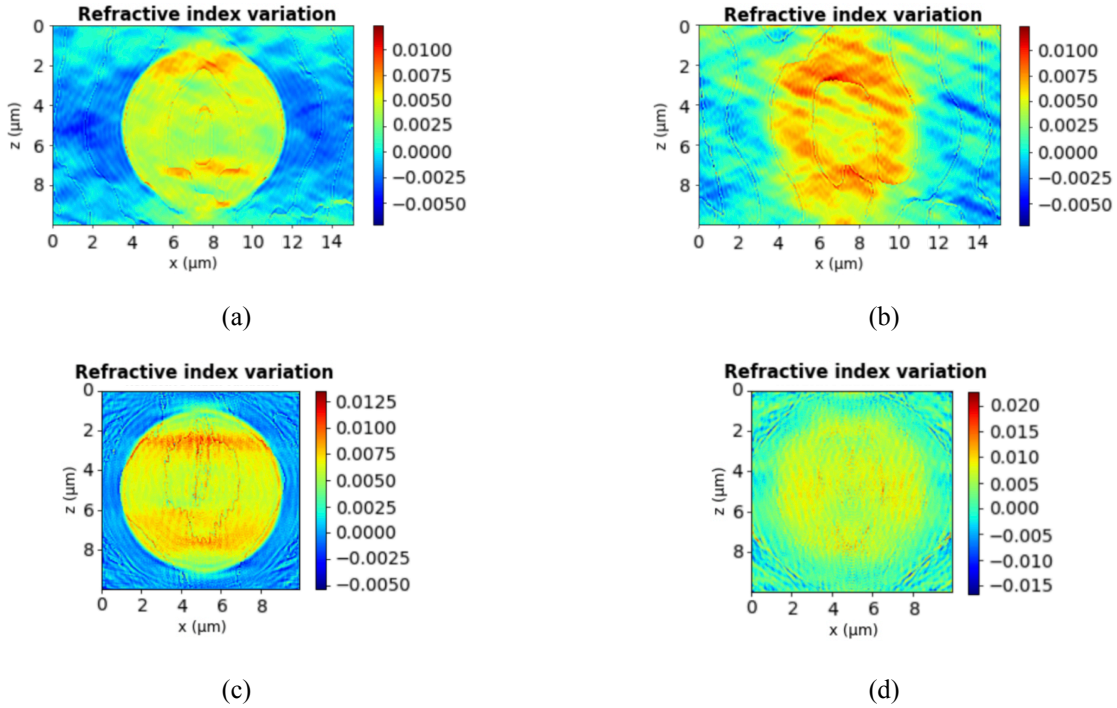

Figure 7: RI cross-section of a fibre core reconstructed from the (a) simulated and (b) measured intensity sinograms using the digital illumination rotation method. RI cross-section of a fibre core reconstructed from the (c) simulated and (d) measured intensity sinograms using the digital specimen rotation method.

Overall, the digital specimen rotation method improves the reconstruction accuracy in terms of the cross-sectional shape by mitigating the missing apple cone problem that elongates the reconstructed RI cross-section, but it provides limited improvement in RI values estimation. Regardless of the types of FBP-based reconstruction strategies, the quality of the reconstructed RI cross-sections remains heavily degraded by reconstruction artefacts.

3.3. Suppression of reconstruction artefacts

Reconstruction artefacts arising from the loss of spectral information were mitigated by applying regularisation to the FBP-based tomographic reconstruction algorithm. TV regularisation was selected over other approaches due to its excellent performance in suppressing noises while preserving structural edges [11]. Equation (13) shows the loss function for the optimisation, which includes an isotropic TV regularisation term. The parameter τ_{TV} is the TV regularisation constant which controls the strength of TV-denoising, with larger values producing stronger noise suppression. Minimising the total loss therefore promotes gradient sparsity of the reconstructed RI cross-section.

$$L_T = \frac{1}{B}\sum_{b=0}^{B}\sum_{n=0}^{N}(I_n - \hat{I}_n)^2 + \tau_{TV}\,|\,\nabla \bullet \Delta n\,| \tag{13}$$

The inclusion of the TV term causes the loss function to be non-differentiable. To address this issue, a proximal gradient descent framework was adopted. The gradient descent step with Nesterov momentum acceleration was replaced by an adaptive moment estimation (ADAM) optimiser, while the non-differentiable term TV term was handled using the Chambolle projection algorithm [12]. The value of τ_{TV} was determined experimentally to be around 0.1. Figure 8 shows the results computed using the proximal optimisation approach. Figures 8(a) and 8(c) show the RI cross-section and the corresponding profile of the fibre core reconstructed from the simulated intensity sinogram, respectively. Figures 8(b) and 8(d) show the corresponding results reconstructed from the measured intensity sinogram.

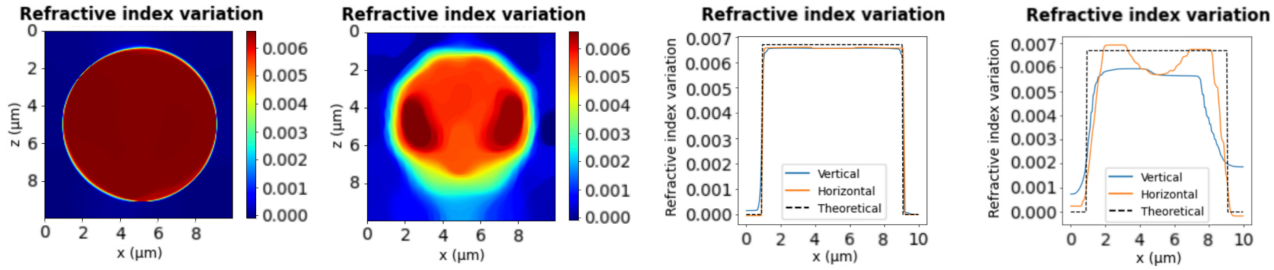

(a) (b) (c) (d)

Figure 8: RI (a) cross-section and (c) profiles of a fibre core computed using the simulated intensity sinogram. RI (b) cross-section and (d) profiles of a fibre core computed using the measured intensity sinogram.

Figures 8(a) and 8(b) show that the application of the proximal gradient descent method with Chambolle projection effectively suppresses the reconstruction artefacts. The reconstructed RI profile in Figure 8(c) closely matches the expected profile when the simulated intensity data are used, demonstrating the effectiveness of the TV regularisation in reducing artefacts and validating the accuracy of the reconstruction algorithm under ideal conditions.

Since both reconstructions in Figures 8(a) and 8(b) use a similar range of illumination angle, the reduction in reconstruction accuracy cannot be attributed solely to the missing cone problem. The regions with higher Δn on the left and right side of the reconstructed RI cross-section in Figure 8(b) exhibit directional dependence, suggesting that they arise from sources of errors that are angle-dependent, in agreement with the results shown in Figure 6(c). Possible cause of this error is optical aberrations in the imaging system or specimen-induced aberrations caused by the fibre cladding. The effect of optical aberrations on the reconstruction accuracy will be investigated in future studies.

4. CONCLUSION

In conclusion, the TIE-based tomography algorithm provides fast and reasonably accurate measurements of Δn distributions. Its performance can be further improved by suppressing reconstruction artefacts using appropriate regularisation techniques. The FBP-based tomographic reconstruction algorithm achieves higher reconstruction accuracy, but the iterative operation reduces computation speed. In addition, careful tunings of algorithm parameters is required to ensure successful optimisation, and convergence to local minima cannot be entirely avoided. Among the two FBP-based approaches, the digital specimen rotation method is more reliable than the digital illumination rotation method, as it mitigates errors introduced by paraxial approximation when propagating light field at an oblique angle. The deviation between the measured and the simulated intensity sinograms increases with increasing illumination angle, indicating an angle-dependent source of systematic error, such as optical aberrations.

ACKNOWLEDGEMENTS

The authors thank Yayasan Khazanah Malaysia and Oxford Centre for Islamic Studies (OCIS) for their continuous support on the student. The authors thank Engineering and Physical Sciences Research Council (EPSRC) (Grant number: EP/W025256/1) for the financial support on this research.

REFERENCES

1. Cacace, T., V. Bianco, and P. Ferraro, *Quantitative phase imaging trends in biomedical applications.* Optics and Lasers in Engineering, 2020. **135**.

2. Aknoun, S., et al., *Quantitative phase microscopy for non-invasive live cell population monitoring.* Scientific Reports, 2021. **11**(1): p. 4409.

3. Douti, D.-B.L., et al., *Quantitative phase imaging applied to laser damage detection and analysis.* Applied Optics, 2015. **54**(28): p. 8375-8382.

4. Bélanger, E., et al., *Comparative study of quantitative phase imaging techniques for refractometry of optical waveguides.* Optics Express, 2018. **26**(13): p. 17498-17510.

5. Barre, N., et al., *Tomographic refractive index profiling of direct laser written waveguides.* Opt Express, 2021. **29**(22): p. 35414-35425.

6. Ma, X., W. Xiao, and F. Pan, *Optical tomographic reconstruction based on multi-slice wave propagation method.* Optics Express, 2017. **25**(19): p. 22595-22607.

7. Chen, M., et al., *Multi-layer Born multiple-scattering model for 3D phase microscopy.* Optica, 2020. **7**(5): p. 394-403.

8. Zuo, C., et al., *Transport of intensity equation: a tutorial.* Optics and Lasers in Engineering, 2020. **135**.

9. Teague, M.R., *Deterministic phase retrieval: a Green's function solution.* Journal of the Optical Society of America, 1983. **73**(11): p. 1434-1441.

10. Moser, S., A. Jesacher, and M. Ritsch-Marte, *Efficient and accurate intensity diffraction tomography of multiple-scattering samples.* Opt Express, 2023. **31**(11): p. 18274-18289.

11. Lim, J., et al., *Comparative study of iterative reconstruction algorithms for missing cone problems in optical diffraction tomography.* Opt Express, 2015. **23**(13): p. 16933-48.

12. Chambolle, A., *An Algorithm for Total Variation Minimization and Applications.* Journal of Mathematical Imaging and Vision, 2004. **20**(1): p. 89-97.